On the Formation of Tropopause Folds and Constituent Gradient Enhancement near Westerly Jets

MATTHEW H. HITCHMAN[a] AND SHELLIE M. ROWE[a]

[a] *Department of Atmospheric and Oceanic Sciences, University of Wisconsin–Madison, Madison, Wisconsin*

(Manuscript received 15 January 2020, in final form 15 April 2021)

ABSTRACT: The role of differential advection in creating tropopause folds and strong constituent gradients near midlatitude westerly jets is investigated using the University of Wisconsin Nonhydrostatic Modeling System (UWNMS). Dynamical structures are compared with aircraft observations through a fold and subpolar jet (SPJ) during research flight 4 (RF04) of the Stratosphere–Troposphere Analyses of Regional Transport (START08) campaign. The observed distribution of water vapor and ozone during RF04 provides evidence of rapid transport in the SPJ, enhancing constituent gradients above relative to below the intrusion. The creation of a tropopause fold by quasi-isentropic differential advection on the upstream side of the trough is described. This fold was created by a southward jet streak in the SPJ, where upper-tropospheric air displaced the tropopause eastward in the 6–10 km layer, thereby overlying stratospheric air in the 3–6 km layer. The subsequent superposition of the subtropical and subpolar jets is also shown to result from quasi-isentropic differential advection. The occurrence of low values of ozone, water vapor, and potential vorticity on the equatorward side of the SPJ can be explained by convective transport of low-ozone air from the boundary layer, dehydration in the updraft, and detrainment of inertially unstable air in the outflow layer. An example of rapid juxtaposition with stratospheric air in the jet core is shown for RF01. The net effect of upstream convective events is suggested as a fundamental cause of the strong constituent gradients observed in midlatitude jets, with the aggregate divergence aloft causing upper-tropospheric air to flow over stratospheric air. Idealized diagrams illustrate the role of differential advection in creating tropopause folds and constituent gradient enhancement.

KEYWORDS: Extratropical cyclones; Mixing; Potential vorticity; Jets; Aircraft observations

1. Introduction

In the introduction to his study of upper-level fronts, Reed (1955) described the benefit of reexamining descriptions of their structure and how they are formed based on new information. He indicated that upper-level fronts are characterized by strong wind shear and can be a source of energy for storm growth. He showed that the tropopause may become folded (Fig. 1a), with an intrusion of stratospheric air sometimes penetrating to near the ground (see his Fig. 13). Figure 1b shows an example of constituent variation across a tropopause fold using dropsonde data (Shapiro 1980). Note the strong contrast between upper-tropospheric and stratospheric air, characterized by high ozone and low amounts of condensation nuclei. Figure 1c shows a section through a cutoff low (Shapiro 1978). Perhaps the most widely accepted paradigm for creating stratospheric intrusions involves the idea of a ‘‘transverse’’ or ‘‘secondary’’ circulation relative to a westerly jet (Sawyer 1956; Eliassen 1962; Hoskins and Draghici 1977), leading to a thin layer of air penetrating downward and equatorward below the jet. This view is summarized in a schematic by Danielsen (1968), reproduced here as Fig. 1d.

In the introduction to Hoskins and Bretherton's (1972) comprehensive paper on analytic representations of frontogenesis, they state that ‘‘there are at least eight mechanisms which may be important in changing temperature gradients and forming atmospheric fronts.’’ Their list does not include (or exclude) the possible role of vertical differences in horizontal advection. Wandishin et al. (2000) included a simple schematic diagram (their Fig. 4c), which suggests that vertical shear of the horizontal wind can cause a tropopause fold, although they did not apply it in their analysis. Some authors have emphasized the 3D nature of how tropopause folds are created (e.g., Bush and Peltier 1994; Rotunno et al. 1994), and how stratosphere–troposphere exchange (STE) occurs (e.g., Sprenger and Wernli 2003). However, to the best of our knowledge, no previous authors have discussed the role of jet streaks, or speed maxima, in creating a tropopause fold by quasi-isentropic differential advection. Numerical models that explicitly integrate vertical motion provide the opportunity to reexamine how tropopause folds are formed. This paper provides a 3D analysis in a nonhydrostatic model of the creation of a tropopause fold around the subpolar jet (SPJ) on the upstream side of a trough.

Over the past decade, we have carried out more than 20 different case studies of westerly jets and midlatitude cyclones using the University of Wisconsin Nonhydrostatic Modeling System (UWNMS), with a focus on dynamical processes in the upper troposphere and lower stratosphere (UTLS). In each case, we found no evidence of a transverse circulation around the jet. Instead, we found that quasi-isentropic differential advection is a common ingredient in tropopause fold formation. Here we present a UWNMS case study, including analysis of aircraft data from research flight 4 (RF04) of the Stratosphere–Troposphere Analyses of Regional Transport (START08) campaign over central North America on 28 April 2008. One

---

Supplemental information related to this paper is available at the Journals Online website: https://doi.org/10.1175/JAS-D-20-0013.1.s1.

Corresponding author: Matthew H. Hitchman, matt@aos.wisc.edu

DOI: 10.1175/JAS-D-20-0013.1

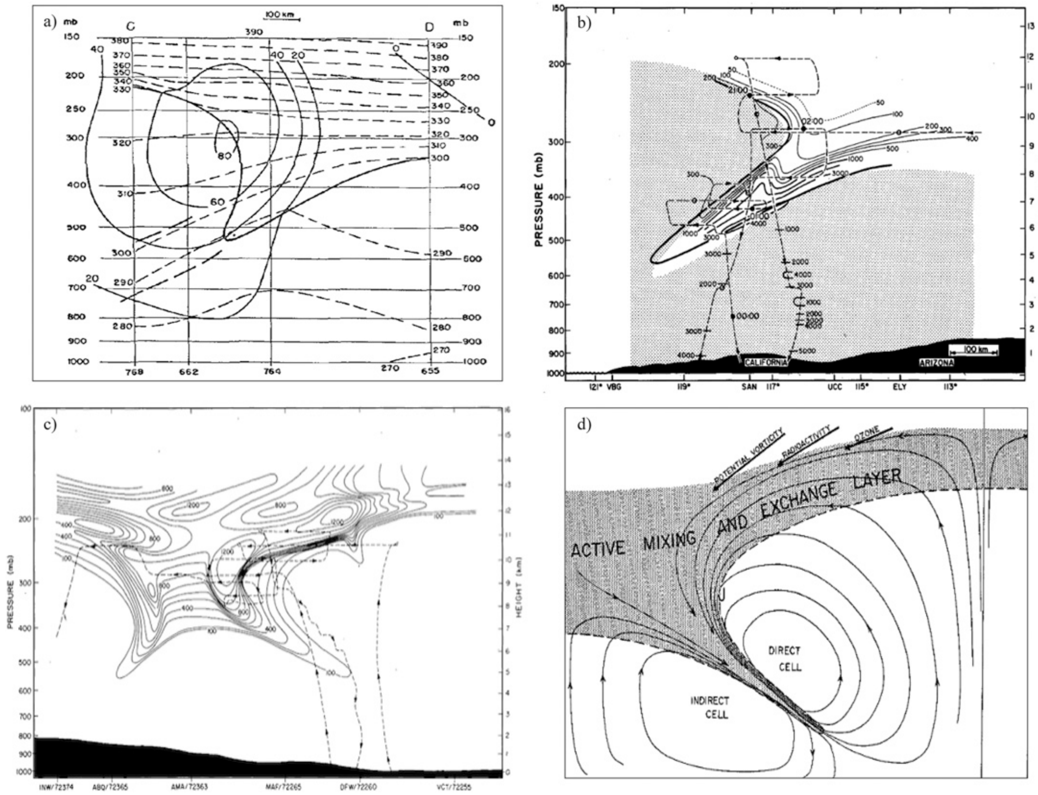

FIG. 1. (a) Zonal section of potential temperature (interval: 10 K) and wind speed (interval: 20 m s^{-1}), with the transition in static stability shown at the tropopause, exhibiting a tropopause fold on the upstream side of a trough over the central United States [Reed's (1955) Fig. 12]. (b) Zonal section of condensation nuclei (particles cm^{-3}) near a southward jet over California derived from aircraft observations [Shapiro's (1980) Fig. 3]. The heavy solid line is the 120 ppbv ozone isopleth. (c) Section from Boulder, Colorado, to Amarillo, Texas, on 29 Mar 1976, showing potential vorticity (10^{-7} K s^{-1} mb^{-1}) [Shapiro's (1978) Fig. 9]. (d) "Schematic of mean circulation relative to the tropopause, including a folded tropopause" [Danielsen's (1968) Fig. 14].

leg of RF04 was particularly useful in that the aircraft sampled the structure of water vapor and ozone in a dive and climb through a stratospheric intrusion and through the core of the SPJ. These data provide useful evidence regarding differential advection and tropopause formation, as well as characterizing constituent gradients between the core of the SPJ and the adjacent stratosphere.

In this paper, we suggest that the fundamental shape of a stratospheric intrusion can be explained by differential advection, where a jet streak (speed maximum) in the SPJ encroaches on the edge of a stratospheric air mass, replacing it with a core of low-PV upper-tropospheric air, overriding high-PV stratospheric air at lower altitudes. The resulting pattern is characterized by a constricted horizontal region of stratospheric air above a broader region of stratospheric air, similar to the patterns shown in Fig. 1.

Thorncroft et al. (1993) include a diagram of idealized transport pathways in midlatitude cyclones, where quasi-isentropic air mass motions can override each other via differential advection in three dimensions, in association with the occlusion process, or Rossby wave breaking (RWB; e.g., McIntyre and Palmer 1983; Hitchman and Huesmann 2007; Sprenger et al. 2007; Martius et al. 2007). Tropospheric air in the warm conveyor belt (WCB; Madonna et al. 2014) can travel cyclonically up and over stratospheric air, leading to a tropopause fold or "double tropopause" structure, which is commonly found poleward of an occluding cyclone (e.g., Randel et al. 2007; Homeyer et al. 2010, 2011a; Martínez-Alvarado et al. 2014). Stratospheric intrusions tend to be turbulent and exhibit a mixed stratospheric–tropospheric chemical signal (e.g., Browell et al. 1987; Zahn et al. 2000; Hoor et al. 2002; Stohl et al. 2003; Bowman et al. 2007; Pan et al. 2007; Hegglin et al. 2008). They often take the form of elongated PV streamers as seen at constant height, and thin sheets as seen in cross sections (Sprenger et al. 2007). Cooper et al. (2004) showed that penetration of stratospheric intrusions by convection can facilitate subsequent mixing into the troposphere. Homeyer et al. (2011b) found that convection into stratospheric intrusions can yield a distinctive mixture of more than 125 ppmv H_2O and 100 ppbv O_3.

Hitchman et al. (2004) showed that when a convective complex penetrated the subtropical jet (STJ) over the east coast of Asia, it induced stratospheric air, with high amounts of ozone, to circulate down around the convection into the middle troposphere, with divergent outflow containing low amounts of ozone overriding the stratospheric air. They estimated a net flux of ozone into the troposphere of ~0.8 Tg O_3 for the event. This process rapidly juxtaposed low ozone with high ozone in the STJ. Studies of summertime convection and the North American monsoon have also discussed the role of convection in juxtaposing lower-tropospheric and stratospheric air (Jourdain et al. 2010; Barth et al. 2012). This theme was emphasized in results from the Deep Convective Clouds and Chemistry (DC3) experiment, which was conducted over the central United States in the summer of 2012 (Pan et al. 2014; Schroeder et al. 2014; Huntrieser et al. 2016a,b; Phoenix et al. 2020). The flights during DC3 did not sample constituent gradients in the SPJ or STJ, and hence these authors did not comment on the cause of strong ozone gradients in the westerly jets.

In addition to describing the role of a jet streak in causing a tropopause fold, in this paper we also investigate the role of deep convection in contributing toward constituent gradients across midlatitude jets, including the role of convectively detrained inertially unstable air into the UTLS. Inertial instability can occur on the equatorward flank of a midlatitude westerly jet in the UTLS (Sato and Dunkerton 2002; Knox and Harvey 2005; Thompson et al. 2018). In studying the "Super Tuesday" midlatitude cyclone of February 2008, Rowe and Hitchman (2015) found regions of negative PV near the tropopause on the anticyclonic shear side of the jet. Their idealized Fig. 11 depicts a stratospheric fold, created by acceleration of UT air in the warm upglide sector, over stratospheric air on the poleward side of the SPJ. Hitchman and Rowe (2017) showed that deep convection generally produces UTLS PV dipoles in midlatitude and tropical cyclones, which are typically sheared into a pair of PV streamers, which merge with the SPJ or STJ. An example of this process is described in this paper, to illustrate the crucial role that upstream convection plays in creating the strong constituent and PV gradients observed in the SPJ during RF04.

RF04 did not sample convection upstream of the stratospheric intrusion. To show how upstream convection can rapidly juxtapose boundary layer air next to stratospheric air, creating a strong constituent gradient near the SPJ, a UWNMS simulation for flight RF01 on 18 April 2008 is shown. RF01 did not sample constituents in the SPJ east of the trough, so aircraft data are not shown for RF01, but the UWNMS simulation is useful to illustrate how convectively transported lower-tropospheric air can be rapidly transported into juxtaposition with stratospheric air in the SPJ. This example, together with results from previous work, is then used to formulate a general argument regarding the role of upstream deep convection in contributing to the strong constituent gradient across the SPJ and to tropopause folds.

Section 2 describes relevant dynamical quantities, the UWNMS simulations, and START08 data. Section 3 provides an overview of RF04 and a description of the formation of a tropopause fold around the SPJ on the upstream side of a trough. Section 4 provides an analysis of water vapor–ozone distributions in the tropopause fold and near the SPJ. The difference in strength between differential advection and mesoscale mixing processes above and below the intrusion, and the cross-jet constituent gradients are discussed. The concept of vertical differences in quasi-isentropic advection also provides a mechanism for superposition of the SPJ and STJ, which is described in section 5. Section 6 shows how deep convection contributes toward enhancing constituent gradients near the jet. Conclusions are given in section 7, which includes schematic diagrams of tropopause fold formation by differential advection and constituent gradient enhancement by convective injection of air into the UTLS.

2. Analysis methods and observations

a. Dynamical quantities

The extratropical tropopause may be defined to occur when the lapse rate is less than 2 K km^{-1}. The extratropical tropopause transition layer includes the lapse rate tropopause, and the regions of sharp upward increase in ozone and PV. It is characterized by ozone mixing ratios in the range 100–200 ppbv, and by values of Ertel's potential vorticity PV $= (1/\rho)(\partial\theta/\partial z)(f + \zeta)$ in the range ~1–2 PVU (1 PVU $= 1 \times 10^{-6}\,\mathrm{m^2\,K\,kg^{-1}\,s^{-1}}$), where ρ is density, θ is potential temperature, $f = 2\Omega\sin\varphi$, and $\zeta = \partial v/\partial x - \partial u/\partial y$ is relative vorticity.

The extratropical UTLS includes the SPJ and STJ, the latter of which climatologically occupies a distinctly higher altitude range. Following Christenson et al. (2017), the two isentropic layers 310–330 and 330–360 K and two PV layers 1–2 and 3–5 PVU are used to highlight motion of the SPJ relative to the STJ. As a further application of the role of differential advection, it will be shown that quasi-isentropic advection can explain jet superposition.

Inertial instability occurs when angular momentum decreases radially outward, as in flow between two rotating cylinders (Rayleigh 1916; Taylor 1923). When this criterion for instability is met, parcels accelerate and rearrange themselves, tending to stabilize the angular momentum profile. In the zonal mean, this condition occurs when total angular momentum increases toward the pole. The classical condition for inertial instability occurs when absolute vorticity is opposite in sign, and larger than the Coriolis parameter for a given hemisphere: $f(f+\xi)<0$ (Eliassen and Kleinschmidt 1957). This criterion is related to Ertel's PV by $f \times \mathrm{PV} = (1/\rho)\,(\partial\theta/\partial z)\,f\,(f + \zeta) < 0$ (Hoskins et al. 1985). In this work, PV < 0 in the Northern Hemisphere is taken to imply inertial instability in the high static stability environment of the UTLS.

b. UWNMS simulations

The UWNMS (Tripoli 1992) has been used to study aircraft field campaigns and transport problems in the UTLS. Recent studies include the role of inertial instability in midlatitude STE and tropopause folds (Rowe and Hitchman 2015), midlatitude "jet flare-ups" (Rowe and Hitchman 2016), UTLS PV dipoles in midlatitude and tropical cyclones (Hitchman and Rowe 2017, 2019), and the role of inertially unstable outflow in a severe flooding event (Rowe and Hitchman 2020).

The resolution for each UWNMS simulation shown in this paper was 20 km × 20 km × 300 m, with a domain ~2000 km

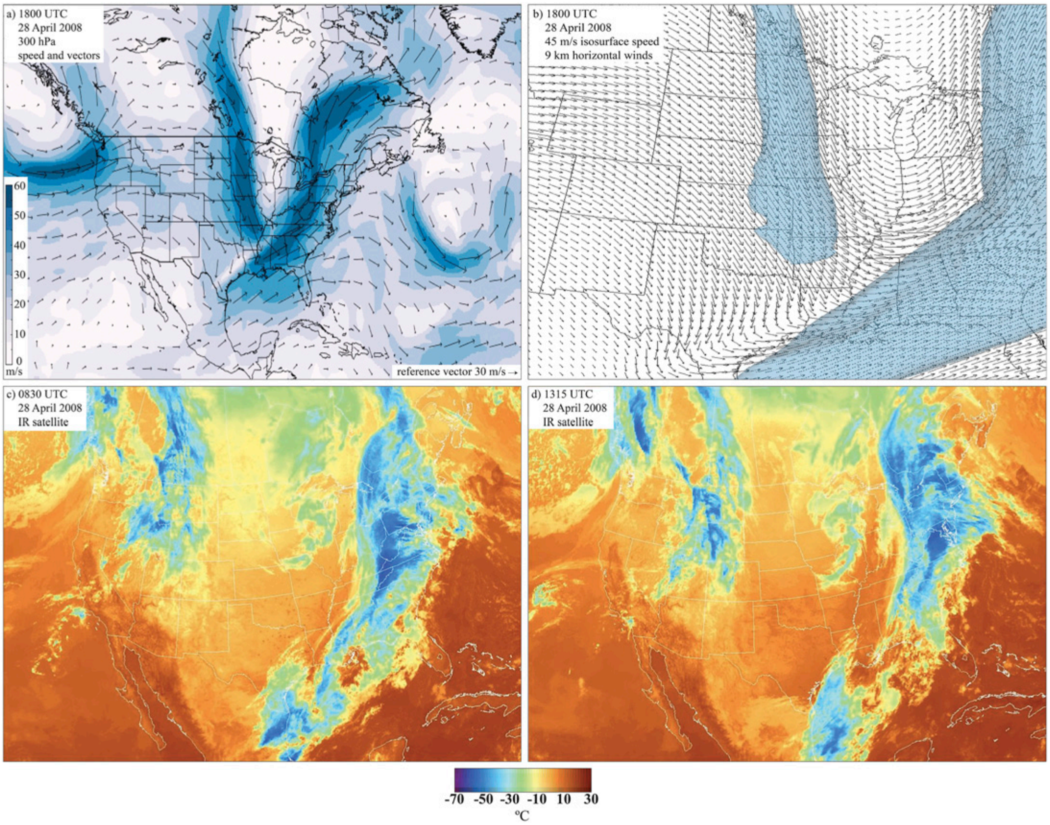

FIG. 2. Synoptic setting for RF04 on 28 Apr 2008: (a) NCEP GFS 300 hPa wind speed (m s^{-1}; color bar) and wind vectors at 1800 UTC 28 Apr 2008; (b) UWNMS 9 km horizontal winds (vectors) and 45 m s^{-1} wind speed isosurface (gray) at 2100 UTC 28 Apr. Cloud-top temperature (°C; color bar) derived from satellite infrared images for (c) 0830 and (d) 1315 UTC 28 Apr 2008.

on a side centered on the flight track over the central United States. The model was initialized by interpolating European Centre for Medium-Range Weather Forecasts (ECMWF) 2.5°-resolution global analyses throughout the volume, and run for 48 h, updating the side boundaries with ECMWF data during integration. Explicit convection was used and model microphysical quantities were treated using the scheme of Hashino and Tripoli (2007). The top of the model was set to 17.6 km, with a 1500 m Rayleigh sponge layer. Vis5d was used to visualize the 3D structure and dynamical features, including particle trajectories.

c. START08 aircraft data

The NSF–NCAR Gulfstream V High-performance Instrumented Airborne Platform for Environmental Research aircraft sampled the UTLS over North America during April–June 2008 in the START08 campaign (Pan et al. 2010). Aircraft meteorological and constituent data were obtained online (http://www.eol.ucar.edu/field_projects/start08), including contemporaneous soundings, satellite images, radar data, and satellite ozone and tropopause height (Pittman et al. 2009). PV along the flight track, available from the START08 website, along with altitude and wind component data, were used to highlight distinct air masses for tracer analysis.

d. NCEP GFS data

The Global Forecast System (GFS) is a global weather forecast model produced by the National Centers for Environmental Prediction (NCEP), with data available from www.emc.ncep.noaa.gov/GFS/doc.php. GFS analyses were used as an independent dataset for illustrating the synoptic situation for each flight. PV values along the flight track were created by the START08 Science Team from GFS analyses.

The infrared satellite images shown in Figs. 2c and 2d were obtained from the image archive meteorological case study selection kit provided by the University Corporation for Atmospheric Research (https://www2.mmm.ucar.edu/imagearchive/).

3. Formation of a stratospheric fold by a jet streak in the subpolar jet

a. Overview of RF04

The GFS 300 hPa analysis and UWNMS 10 km winds for 1800 UTC 28 April 2008 are shown in Figs. 2a and 2b. A trough is seen to be entering the Pacific Northwest, with a ridge extending from northern Mexico along the Rockies into Canada, and a meridionally elongated trough over the Great Lakes. In the SPJ to the west of this trough, a southward jet streak, with

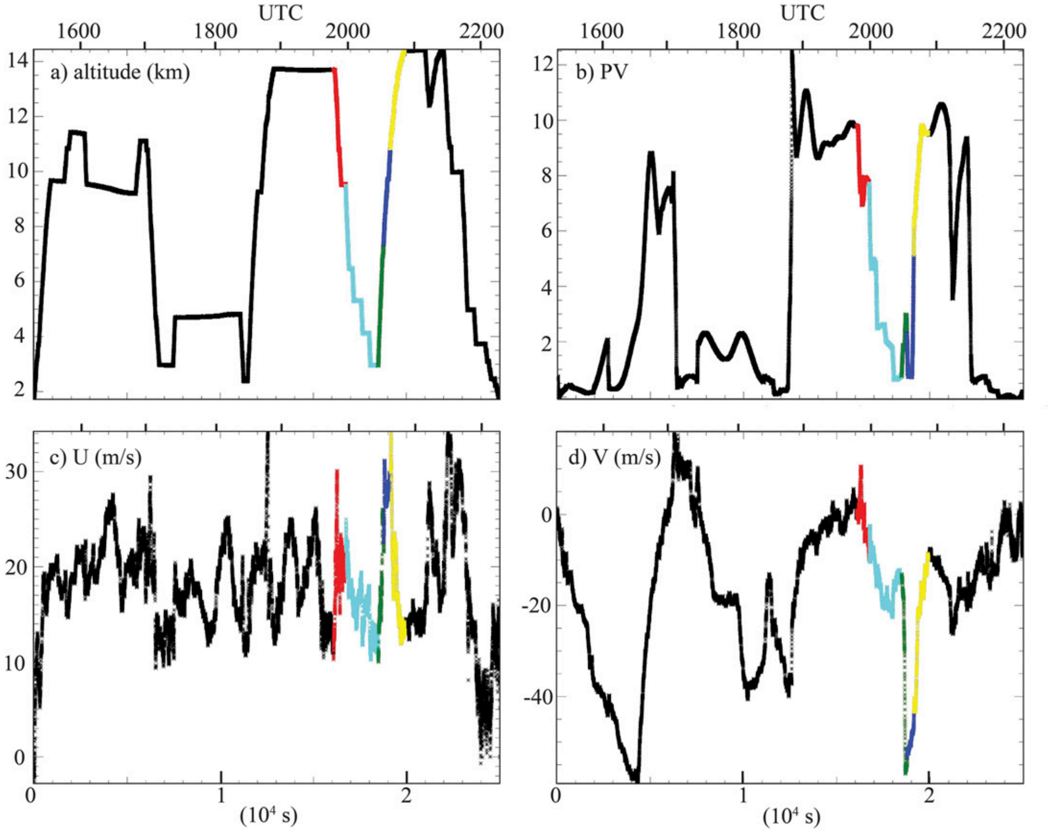

FIG. 3. Gulfstream V flight-track variables as a function of time (10^4 s) for RF04, from takeoff at 1520 UTC to landing at 2215 UTC 28 Apr 2008: (a) aircraft altitude (km), (b) GFS PV (PVU), and aircraft-derived (c) zonal wind (m s^{-1}) and (d) meridional wind (m s^{-1}). The period 1946–2054 UTC is investigated in detail in Fig. 6, with flight segments identified by color, where red is descent in the lower stratosphere, light blue is descent through stratospheric intrusion, green is ascent through intrusion, dark blue is ascent through SPJ, and yellow is ascent in lower stratosphere. Thicker tick marks on the upper side of each panel indicate time in UTC.

speeds exceeding 40 m s^{-1}, is observed extending from Manitoba to Arkansas (Figs. 2a,b). This jet streak plays a central role in creating a tropopause fold on the upstream side of the trough. Note also the STJ extending from the Gulf of Mexico to Quebec (Figs. 2a,b). Inspection of maps of tropopause pressure and 200 hPa ozone derived from satellite data at 1930 UTC 28 April 2008 (not shown) reveal that tropopause pressures reach ~220 hPa in the ridge over Montana and ~320 hPa in the trough over the Great Lakes, while 200 hPa ozone values ranged from ~180 ppbv in the ridge to ~500 ppbv in the trough.

Satellite cloud-top temperature maps are shown for 0830 UTC and 1315 UTC 28 April 2008 in Figs. 2c and 2d. During the period leading up to RF04, widespread convection may be seen over California, Nevada, Utah, Colorado, and Wyoming. The 300 hPa chart for 1800 UTC (Fig. 2a) suggests that boundary layer air injected by convection into the UTLS would be advected eastward toward the trough over the central United States. The boundary layer in this area of the western United States is relatively uncontaminated by urban pollution and might be expected to have ozone values less than 50 ppbv.

The flight track for RF04 was along an east–west section near 40°N. The Gulfstream V took off from Broomfield, Colorado, at ~1520 UTC [0920 mountain daylight time (MDT)] and landed at ~2215 UTC (1615 MDT) 28 April 2008. During the 6 h 55 min flight, the aircraft flew eastward to Indianapolis, Indiana, and back twice, including three ascents into the lower stratosphere (Fig. 3a). The corresponding values of PV, u, and v during this flight are shown in Figs. 3b–d.

During the interesting period 1946–2054 UTC [~1500–1600 central daylight time (CDT)], indicated by colored segments in Fig. 3a, the aircraft transected the intrusion during descent, ascended through the stratospheric filament, then through the core of the SPJ. The geographical location of this portion of RF04 is shown as a heavy blue line in Fig. 4d. The projection of the colored portion of the flight track onto a zonal–altitude section of UWNMS PV at 2200 UTC is shown in Fig. 5b. This provides a representation of the location of each flight segment relative to the stratospheric intrusion and SPJ. The storm structure propagated slightly eastward and mostly southward as the aircraft moved through it during this ~1 h of the flight. Each of the color segments in Fig. 3 correspond to specific panels displaying water vapor and ozone data in Fig. 6, plotted in the corresponding color for each segment. Figure 7 shows the evolution of the momentum pulse in the SPJ at 8.5 and 12 km, with the corresponding cross sections in Fig. 8 illustrating jet superposition by differential advection. Figure 9 shows UWNMS vertical motion at 8.5 km altitude, which indicates that the SPJ is embedded in air with uniform weak descent.

The V-shaped flight segment in Fig. 5b has been copied onto Fig. 6b to illustrate the westward progression of the colored segments with time along the flight. The arrows in Fig. 6 indicate the direction of motion of the flight in H_2O–O_3 space. The aircraft first sampled the lower stratosphere (red segment, 12 min in duration, 1946–1958 UTC), starting at 13 700 m (~10 PVU) over Indianapolis near 86.3°W and descending to 9528 m (~8 PVU) at ~88.1°W, passing through a minimum in water vapor (Fig. 6a). It continued descending westward to the base of the stratospheric intrusion (light blue, 29 min, 1958–2027 UTC) to 2955 m (~1 PVU) over Hannibal, Missouri, near 91.4°W (Fig. 6b).

The aircraft then ascended through the intrusion (green, 5 min, 2027–2032 UTC), reaching maximum ozone (~170 ppbv) and ~2.5 PVU near 5.0 km, and emerging out the top of the intrusion at 6500 m (~2.0 PVU) (Fig. 6c). The aircraft then ascended through the jet core near 8 km (~1 PVU), with maximum southward flow of ~58 m s^{-1} (Fig. 3b), and into the upper troposphere (dark blue segment, 6 min, 2032–2038 UTC) (Fig. 6d). Note the decrease in PV going above the jet core prior to entering the stratosphere (Fig. 3b). The final segment sampled the lower stratosphere from 11 000 m (~5 PVU) to 14 500 m (~10 PVU) (yellow segment, 16 min, 2038–2054 UTC) (Fig. 6e), just west of Saint Joseph, Missouri, near 95.4°W. Figure 6f shows measurements of air with speed exceeding 44 m s^{-1} for the full duration of RF04.

b. *Tropopause fold formation on the upstream side of the trough during RF04*

The development of a tropopause fold associated with the jet streak in the southward SPJ is shown in Figs. 4 and 5, from near the beginning (1640 UTC) to near the end (2200 UTC) of RF04 on 28 April 2008. The evolution of PV and streamfunction at 4, 6, and 8 km altitude is shown in Fig. 4. Figures 5a and 5b show zonal cross sections of wind speed and PV along axis a–a′ in Figs. 4c and 4d, while Figs. 5c and 5d show meridional sections along axis b–b′ in Figs. 4c and 4d through the southward jet core.

The eastward tilt with height of the west edge of the stratospheric intrusion is highlighted in Fig. 4 by the 1 PVU contour at 6 km superimposed as a dashed line at 4 and 8 km altitude. Note how the pattern of tropospheric air at 8 km overlapping stratospheric air at 6 km propagates southward with time (cf. left and right images). This is the signature of an evolving tropopause fold. At 1640 UTC (left) the trough axis, as seen in the pattern of horizontal streamlines, extends from Lake Michigan to Alabama. By 2200 UTC (right) the southern half of the trough axis had moved eastward toward Georgia. The western edge of the stratospheric PV maximum receded eastward more quickly with increasing altitude (Fig. 4). At 1640 UTC the 1 PVU contour at 4 km is located slightly west of that at 6 km and at 8 km (Figs. 4a,c,e). By 2200 UTC (Figs. 4b,d,f), the west edge of the 1 PVU contour was located over western Iowa at 4 km, central Iowa at 6 km, and eastern Iowa at 8 km, consistent with the enhancement of the fold shown in Figs. 5a–d.

At 1640 UTC (1140 CDT) a southward SPJ exceeding 50 m s^{-1} is seen on the west flank of the stratospheric intrusion (Fig. 5a). It is in a similar configuration to Fig. 1a from Reed (1955). The 1–2 and 3–5 PVU layers are highlighted in purple and green shading, respectively. The 1 PVU contour runs vertically through the jet core, approximately dividing air poleward and equatorward of the wind maximum at each level. This southward jet streak centered near 9 km altitude is also moving eastward, with tropospheric air in the 7–10 km layer displacing stratospheric air in that layer and overriding the more slowly moving stratospheric air in the 4–6 km layer. By 2200 UTC (1600 CDT) a clear signature of a tropopause fold has emerged (Fig. 5b), with the SPJ overlying a layer of stratospheric air. This classical signature of a tropopause fold as shown in PV and wind speed (Fig. 5b) is similar to those shown in Figs. 1b and 1c.

Figures 5c and 5d shows the corresponding sequence of meridional sections, oriented along axis b–b′ in Fig. 4. Note the southward progression of the speed maximum and displacement of air with PV exceeding 1 PVU in the layer 6–10 km, overriding a portion of the stratospheric intrusion in the 3–5 km layer. The approach of the low-PV air in the southward SPJ acts to enhance the buckled pattern in PV on the poleward flank of the STJ, sharpening the stratospheric intrusion in this location (cf. Figs. 5c,d).

The formation and evolution of this tropopause fold are shown in online supplemental movies S1 and S2, highlighting PV in blue and wind speed in black, as seen in oblique views from the southwest and south, respectively. Note how low-PV air replaces high-PV air in the upper portion of the stratospheric intrusion in association with the jet streak, but not in the lower portion of the intrusion, causing a tightening or ''carved out'' region, yielding a classical tropopause fold.

4. Distribution of water vapor and ozone in a stratospheric fold and the SPJ during RF04

Pristine boundary layers may have ozone concentrations of less than 35 ppbv, while polluted boundary layers can have much higher values. During RF04, water vapor mixing ratios diminished upward by about three orders of magnitude from ~2300 ppmv in the lower troposphere to ~6 ppmv in the stratosphere, while ozone ranged from ~900 ppbv in the lower stratosphere to ~35 ppbv in the jet core. We hypothesize that the existence of low water vapor and very low ozone in the core of the SPJ can be explained by detrainment of air from deep thunderstorms upstream, which ingested pristine boundary layer air with low ozone, and rapidly dehydrated during ascent, by condensation and precipitation. If the time scale for the production of tracer gradient by differential advection is shorter than the time scale by which it is removed by mixing, a sharp corner, or transition across an air mass boundary, would be expected. Each segment of the dive and ascent is now described in detail.

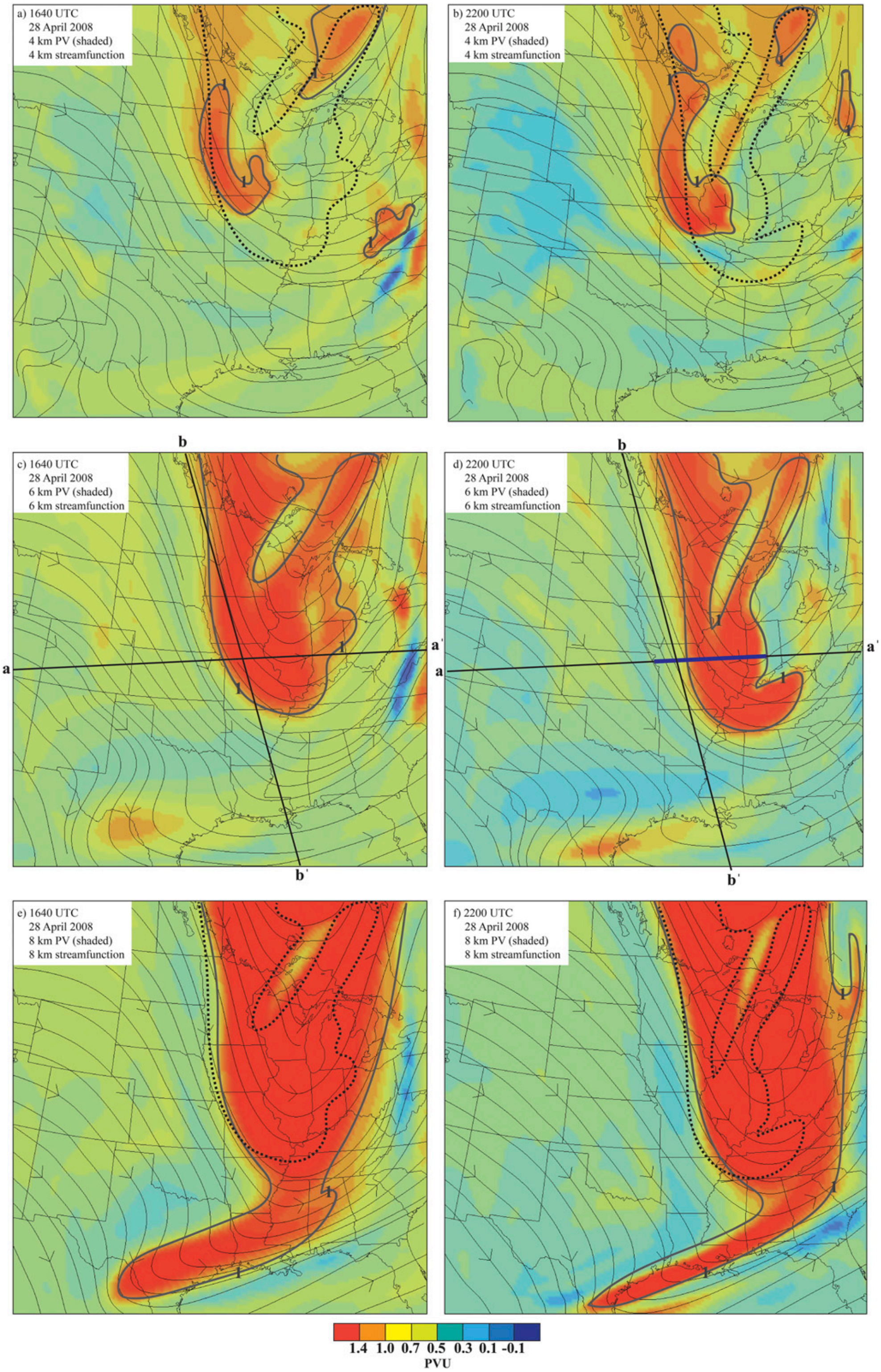

FIG. 4. Synoptic evolution from (left) 1640 to (right) 2200 UTC 28 Apr 2008 of UWNMS horizontal streamfunction and PV (color bar) at (a),(b) 4, (c),(d) 6, and (e),(f) 8 km altitude. The 1 PVU contour is emphasized in thick gray at each level. The 1 PVU contour at 6 km is transcribed onto the 4 and 8 km charts as dashed lines at each time to illustrate the eastward tilt with height of the tropopause. The locations of zonal section a–a′ (Figs. 5a,b) and meridional section b–b′(Figs. 5c,d) are indicated in (c) and (d). The location of the aircraft during 1946–2054 UTC is shown as a heavy blue line in (d).

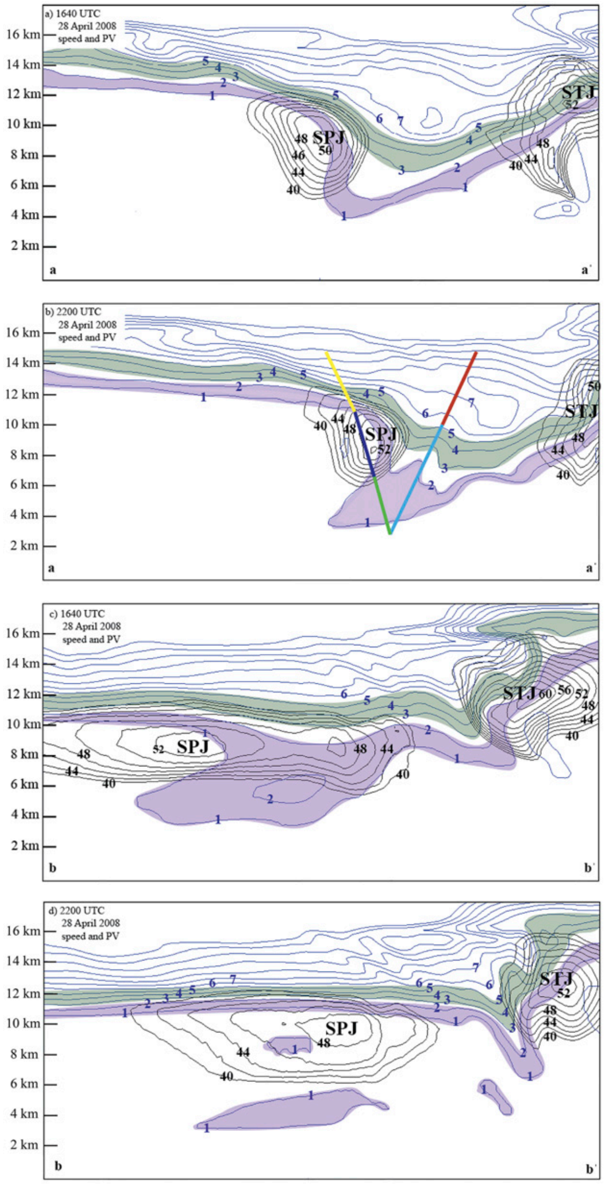

FIG. 5. Sections showing the development of a tropopause fold in the UWNMS during RF04 from 1640 to 2200 UTC 28 Apr 2000, with blue PV contours (every 1 PVU above 1 PVU) and black wind speed contours (every 2 m s^{-1} above 40 m s^{-1}) in (a),(b) zonal sections along axis a–a′ and (c),(d) meridional sections along axis b–b′ in Figs. 4c and 4d. The 1–2 PVU layer (with SPJ) and 3–5 PVU layer (with STJ) are highlighted with light purple and green shading, respectively. The location of the Gulfstream V in this zonal section during 1946–2054 UTC is shown as colored segments along a V-shaped path in (b).

a. Descent through the hygropause

Figure 6a shows the initial descent in the lower stratosphere (red segment in Figs. 3, 5b, inset in 6b), where a classical C-shaped profile of water vapor versus ozone is observed. Starting from ~13.7 km (~10 PVU) at 1908 UTC, ozone mixing ratios of ~900 ppbv coincide with moderate values of water vapor (~11 ppmv). Descending to ~9.6 km (~8 PVU), water vapor reaches a minimum (hygropause) near 8 ppmv and is highly variable in the lowest stratosphere (ozone < 500 ppbv).

In the tropical lower stratosphere, the minimum in water vapor is ~2–4 ppmv. Formed in association with deep convection, this layer of lower water vapor is transported quasi-isentropically into the midlatitudes by plumes of poleward motion, which constitute the poleward branch of the Brewer–Dobson circulation (Randel and Jensen 2013; Schoeberl and Dessler 2011; Schoeberl et al. 2018). In the midlatitudes, water vapor increases downward into the UTLS, where there is enhanced mixing with moisture-rich tropospheric air. The spread in the lowest stratosphere in Fig. 4a is related to the magnitude of these mixing processes.

b. Descent and ascent through the stratospheric intrusion

Descent to the base of the stratospheric intrusion at ~3 km (~1 PVU) is shown in Fig. 6b (blue segment in Figs. 3, 5b), where ozone decreases from ~400 to ~60 ppbv, and water vapor increases from ~10 to ~1200 ppmv. The spread of points increases downward. The rounded corner is consistent with relatively efficient mixing processes within the lower stratosphere.

Figure 6c shows the portion of the flight track ascending through the intrusion from ~3 to 6.5 km (green segment in Figs. 3, 5b). The intrusion lies beneath the southward SPJ (inset, Fig. 6b). Starting from near 3 km (~1 PVU), moderate ozone values of ~60 ppbv are seen, along with water vapor values of ~1000 ppmv. At first water vapor decreases upward to ~220 ppmv, with ozone constant at ~50 ppbv. Ascending toward the center of the fold, water vapor gradually decreases to ~50 ppmv, while ozone increases to ~180 ppbv near the core of the fold at 5 km (top-left corner in Fig. 6c). From the center of the intrusion to its upper edge, ozone decreases monotonically to ~50 ppbv, with water vapor values less than ~80 ppmv (lower-left corner in Fig. 6c). Near the top of the intrusion (lower-left corner in Fig. 6c), a shallow layer of enhanced water vapor is found, reaching ~250 ppmv, with ozone ~45 ppbv. Another shallow layer of enhanced water vapor is encountered above the stratospheric intrusion, approaching the jet core (Fig. 6d).

The transition above the core of the intrusion is sharper than the transition below the core, which may be related to the rapidity of gradient enhancement by differential advection associated with the vertical shear below the jet. This difference may also be consistent with enhanced mixing processes along the bottom of and within the intrusion, as found by Homeyer et al. (2011b). The sharpness of the ozone peak in the upper left of Fig. 6c and of the water vapor spike in the lower left of Fig. 6c suggest that the time scale for advection of these layers relative to adjacent layers is less than the time scale for reduction of constituent gradients by mesoscale mixing.

c. Ascent through the core of the SPJ

The portion of the flight ascending through the jet core into the upper troposphere, from ~6.5 to 11 km (dark blue segment in Figs. 3, 5b), is shown in Fig. 6d. Upon emergence from the upper edge of the intrusion near 70 ppmv H_2O, 63 ppbv O_3 in Fig. 6d (cf. last point in Fig. 6c), ozone decreases upward while moisture increases until a moist layer is encountered just below the jet, reaching ~185 ppmv and ~46 ppbv ozone (Fig. 6d). Ascending out of the top of the moist layer, water vapor

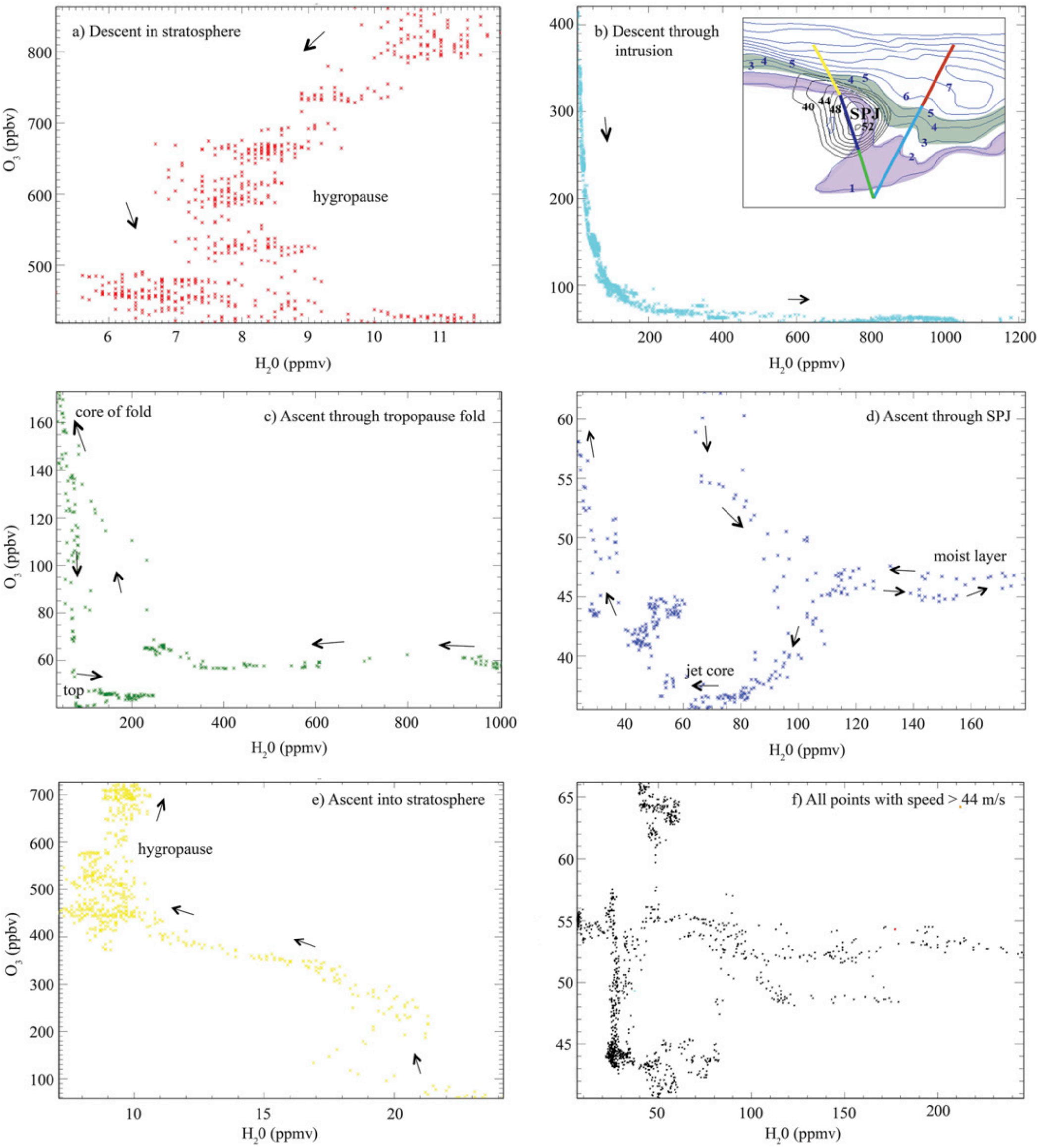

FIG. 6. Observed values of water vapor (ppmv) and ozone (ppbv) during RF04 for the selected flight segments shown in Fig. 3: (a) 1946–1958 UTC, red, descent in the lower stratosphere; (b) 1958–2027 UTC, light blue, descent through stratospheric intrusion; (c) 2027–2032 UTC, green, ascent through intrusion; (d) 2032–2038 UTC, dark blue, ascent through SPJ; (e) 2038–2054 UTC, yellow, ascent into lower stratosphere; and (f) data near the SPJ for the entire flight RF04, 1520–2215 UTC 28 Apr 2008, black, all points with speed exceeding 44 m s^{-1}. The inset in (b) shows the colors for specific flight segments reproduced from Fig. 5b, corresponding to the colors shown in each panel.

gradually decreases upward, while ozone reaches a distinct minimum of ~35 ppbv in and just above the jet core. Above the jet core, water vapor continues to decrease to ~20 ppmv, as ozone increases to ~60 ppbv before entering the stratosphere. This profile is consistent with injection of relatively pristine boundary layer air containing low ozone values directly into the UTLS, coinciding with low PV on the equatorward side of the jet.

d. Ascent into the stratosphere

Rising into the lower stratosphere from ~11 km to ~14.5 km (Fig. 6e, yellow segment in Figs. 3, 5b), water vapor drops from ~30 to ~10 ppmv, while ozone increases from ~100 to ~400 ppbv. The layer 450–700 ppbv ozone coincides with the minimum in water vapor (Figs. 6a,e).

e. Water vapor and ozone values in the SPJ for entire flight RF04

Figure 6f shows water vapor–ozone pairs for the entire flight, including all times when the southward wind speed exceeded 44 m s^{-1}. These include points in the lower-left corner of Fig. 6c, all of the points in Fig. 6d, and earlier flight legs through the SPJ. Minimum values of ozone in the

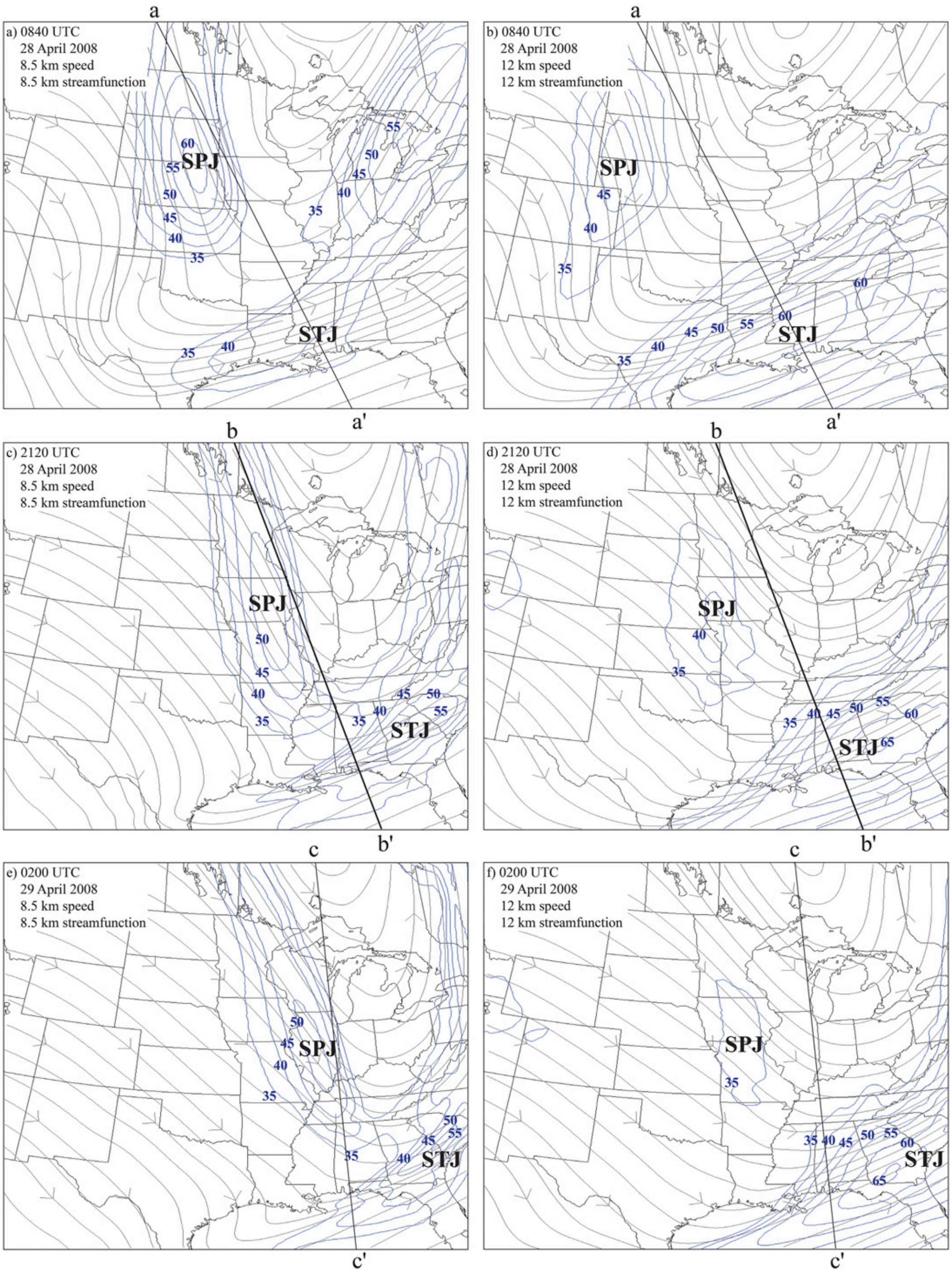

FIG. 7. Sequence of plan views of UWNMS streamfunction and wind speed (blue contours every 5 m s^{-1} from 35 m s^{-1}) at (left) 8.5 and (right) 12 km showing superposition of the SPJ and STJ: (a),(b) 0840 UTC 28 Apr, (c),(d) 2120 UTC 28 Apr, (e),(f) 0200 UTC 29 Apr. Note that the SPJ is prominent at 8.5 km, while the STJ is prominent near 12 km. Meridional sections shown in Fig. 8 are indicated as a–a′, b–b′, and c–c′.

jet are ~35 ppbv, but considerable variation is observed within the jet, perhaps representative of the initial mixing stages of thin sheets of air superimposed by differential advection.

The L-shaped structure in the lower-left corner of Figs. 6c and 6f occurs at the top of the stratospheric intrusion, consistent with rapid advection of constituents in the SPJ relative to stratospheric air. In the jet core, values of PV are close to zero (compared with 2–3 PVU poleward of the jet), values of ozone are ~35 ppbv (compared with 200–300 ppbv in the adjacent stratosphere), and values of water vapor are generally less than 60 ppmv (quite small compared with most of the troposphere). Section 6 discusses how these constituent gradients can be produced by detrainment from upstream convection.

5. Jet superposition by quasi-isentropic differential advection

A sequence of plan views (Fig. 7) and vertical sections (Fig. 8) of wind speed, streamlines, and potential temperature illustrates the superposition of the STJ and SPJ, which occurred during the afternoon and evening of RF04. Their relative motion occurred quasi-isentropically. The air mass in which the SPJ is embedded sinks uniformly at ~2 cm s^{-1} as it moves equatorward, with no evidence of a secondary circulation (Fig. 9).

In an analysis of 50 boreal winters, Christenson et al. (2017) provided a useful assessment of the statistical occurrence for the isentropic locations of the STJ and SPJ. They determined that the potential temperature layers 340–355 and 315–330 K were most appropriate for distinguishing between the two jets. This nomenclature was used by Winters and Martin (2016, 2017), who investigated the role of transverse circulations and superposition of PV structures in causing jet superposition. In this paper, we suggest that jet superposition can occur simply by differential advection. Since RF04 occurred in late April, we modify the criteria of Christenson et al. (2017) slightly and categorize the STJ as the 330–360 K layer and the SPJ as the 310–330 K layer (green and purple layers, respectively, in Fig. 8).

Figure 7 shows the evolution of horizontal streamlines, the SPJ maximum near 8.5 km (left), and the STJ maximum near 12 km (right), together with the locations of the meridional sections shown in Fig. 8. After experimenting with various angles for the sections along the SPJ we found that results shown in Fig. 8 are fairly insensitive to the choice of angle. At 0840 UTC 28 April (Figs. 7a,b, 8a), there is a clear distinction between the SPJ, which maximizes at ~60 m s^{-1} over South Dakota near 8.5 km, and the STJ, which maximizes at ~60 m s^{-1} over the Gulf Coast near 12 km altitude. The centers of these two jets are located ~2.5 km apart vertically and ~1000 km apart horizontally, separated by a region with wind speeds less than 30 m s^{-1}.

By 2120 UTC 28 April (Figs. 7c,d, 8b), a portion of the SPJ had undercut the STJ, establishing jet superposition. By 0200 UTC 29 April (Figs. 7e,f, 8c), this overlap had increased considerably. A comparison of isentropes and streamlines in Figs. 8c and 8d shows that the motion of the SPJ and STJ cores is quasi-isentropic. Note the reduction in strength with time of the SPJ as seen at 12 km (Figs. 7b,d,f), consistent with quasi-isentropic equatorward descent.

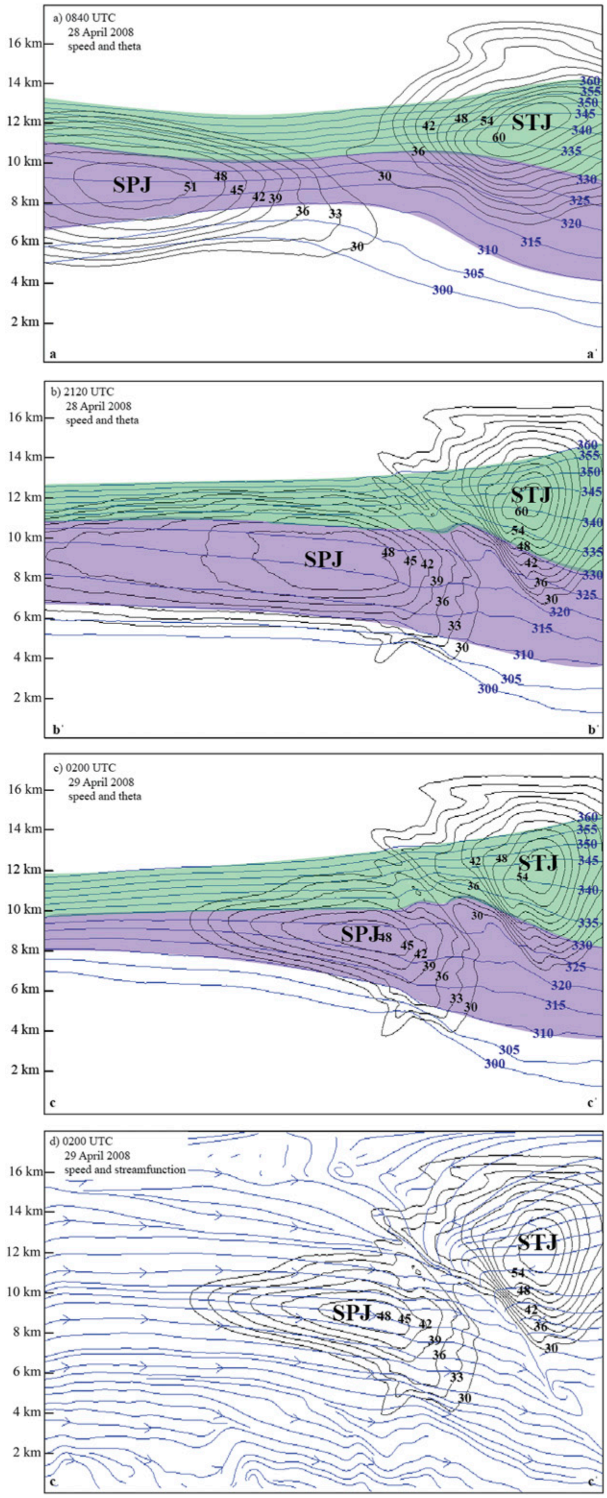

FIG. 8. Sequence of meridional sections of UWNMS potential temperature (blue contours, 300–360 K, every 5 K) and wind speed (black contours, 30–60 m s^{-1}, every 3 m s^{-1}) showing the superposition of the SPJ and STJ that occurred during RF04: (a) 0840 UTC 28 Apr (section a–a′ in Figs. 7a,b), (b) 2120 UTC 28 Apr (section b–b′ in Figs. 7c,d), and (c) 0200 UTC 29 Apr

←

(section c–c′ in Figs. 7e,f). In (a)–(c), the isentropic layer 310–330 K (SPJ) is shaded in purple, while the layer 330–360 K (STJ) is shaded in green. (d) As in (c), but showing streamlines in the plane instead of potential temperature.

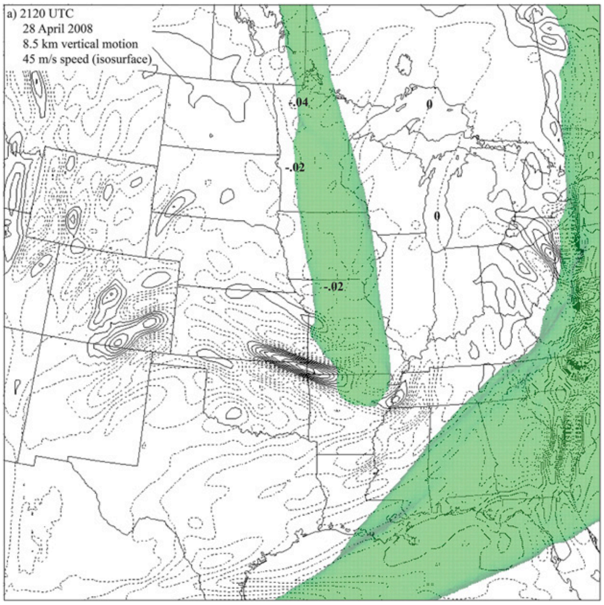

FIG. 9. Vertical motion (contours every 0.01 m s^{-1}, negative dashed) and 45 m s^{-1} speed isosurface (green) at 8.5 km altitude in the UWNMS at 2120 UTC 28 Apr 2008.

A striking pattern of convergence in meridional streamlines is seen between the two jets (Fig. 8d). The southeastward motion of air associated with the SPJ is deep, as is the northeastward-moving layer of air containing the STJ, both of which extend into the lower stratosphere. This convergence of air masses is related to a noticeable buckling pattern in contours between the two jets, consistent with generation of gravity waves. This sequence shows that a straightforward mechanism for jet superposition is simply quasi-isentropic differential advection between two layers. In this case, the superposition is fundamentally related to a south-southeastward jet streak in the SPJ in the 310–330 K layer, which was moving in a different direction relative to the STJ.

Figure 9 shows the distribution of UWNMS vertical motion at 8.5 km, together with the 45 m s^{-1} speed isosurface, at 2120 28 April 2008, which may be compared with Figs. 7c, 7d, and 8b. The SPJ is embedded in a broad air mass that is descending at ~2 cm s^{-1}. Values of vertical velocities are small and of the same sign on both sides of, and within the SPJ. The southward-propagating momentum surge in the SPJ excites a field of gravity waves at its leading edge, similar to a bow wake. This is consistent with the Rossby adjustment process, where a poleward surge in the WCB, or an equatorward surge of air to the west of a trough, commonly excites a field of gravity waves (cf. Fig. 3 of O'Sullivan and Dunkerton 1995).

6. Convective transport of lower-tropospheric air into the SPJ

During RF04, ozone values of ~35 ppmv were observed in the SPJ. We hypothesize that this air was injected into the SPJ by convection upstream of the adjacent ridge. Figures 2c and 2d show that convection was located upstream preceding RF04. To further demonstrate this process, we investigate an analogous situation with closer proximity between the jet and convection. During RF01, robust convection occurred in the warm sector immediately to the east of the elongated narrow trough, or stratospheric filament, which was simulated with the UWNMS.

Figure 10 shows the upper-tropospheric synoptic setting at 1320 UTC 18 April 2008 in the UWNMS, together with the location of the meridional section shown in Fig. 11. At 8.7 km, a stratospheric PV filament extends from Ontario to Texas, with a "fiddle-head" or rolled-up PV maximum over Oklahoma (Fig. 10a). On its east edge the poleward and eastward-arcing jet exceeds 40 m s^{-1} (Fig. 10b). The −1 PVU isosurface (dark blue) indicates regions of inertially unstable air in the UTLS, which are found in the convective WCB over Minnesota and Wisconsin, just to the east of the stratospheric air mass (Figs. 10a,b). These locations represent air that has been ingested into thunderstorms and injected into the upper troposphere along the equatorward flank of the SPJ.

The warm upglide sector to the south and east of a midlatitude trough is often characterized by outbreaks of deep convection. Deep convection can generate regions of PV dipoles in the UTLS, which are often sheared into negative–positive PV filament pairs, and can create regions of negative PV along the equatorward side of the jet (Rowe and Hitchman 2015, 2016; Hitchman and Rowe 2017). Convection was also found by Harvey et al. (2020) to make a significant contribution to the creation of negative PV streamers on the jet flank over the North Atlantic.

Figure 11 presents meridional sections of UWNMS PV, streamlines, and the location of the SPJ jet for 1320 UTC 18 April during RF01, along y–y′ in Fig. 10, which transects a negative PV anomaly and a stratospheric PV filament over northeastern Minnesota. Due to its altitude range, this speed maximum is identified as the SPJ. Figure 11a shows the signature of a stratospheric PV anomaly north of the SPJ, which extends down to ~4 km altitude. The poleward jet maximum on the eastern flank of the PV anomaly (Fig. 11a) is embedded in a deep layer (~4–12 km) of poleward flow (Fig. 11b). Note that, in this case also, there is no indication of a secondary circulation associated with the jet (Fig. 11b). Instead, the stratospheric intrusion exhibits a slight indentation on its east side (Fig. 11a), where the poleward SPJ advected upper-tropospheric air near 9 km over more stagnant stratospheric air near 8 km. This is consistent with the hypothesis that differential advection can create a tropopause fold. Together with analysis of RF04 in the equatorward SPJ, this helps to complete a depiction of how the east–west symmetry of the shape of a stratospheric intrusion can be created in a cutoff low (Fig. 1c).

Figure 12 shows oblique views, from the south and southeast, of the 45 m s^{-1} speed isosurface and −1 PVU surface at 1320 UTC 18 April 2008 in the UWNMS. It includes two 26-h trajectories, one of which (purple) passes through the negative PV anomaly and the other (green) passes through the jet maximum in the UTLS over the upper Mississippi valley. A few hours before this time, a region of convection broke out

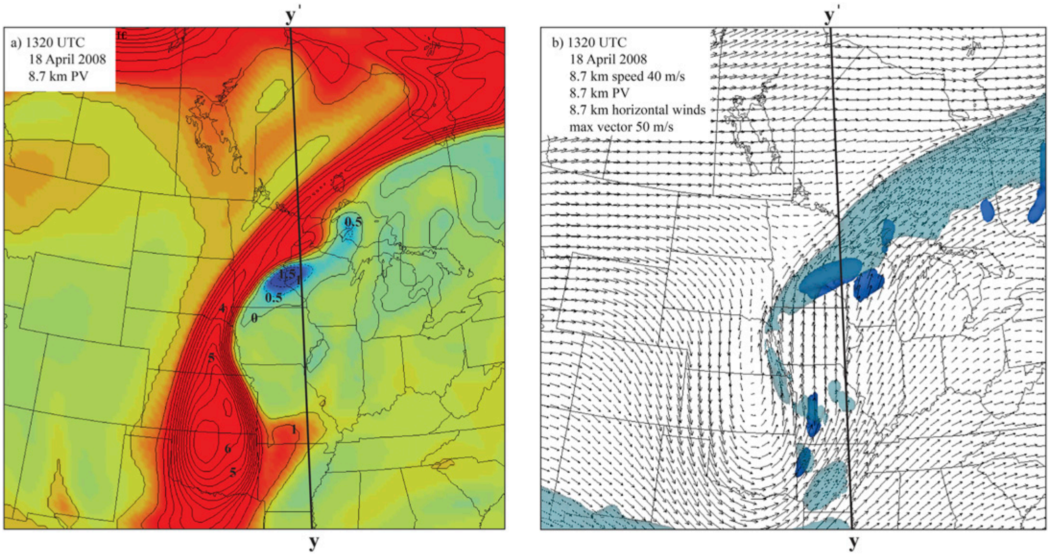

FIG. 10. Plan views at 8.7 km in the UWNMS at 1320 UTC 18 Apr 2008 of (a) PV (color fill, blue negative, with black contours every 1 PVU) and (b) horizontal wind vectors (max vector: 50 m s^{-1}), speed isosurface of 40 m s^{-1} (silver), and PV isosurface of −1 PVU (blue). The meridional section shown in Fig. 11 is indicated with the line y–y′.

over northeastern Oklahoma. The purple trajectory extends from the boundary layer, up and over the yellow trajectory (Fig. 12b), indicating that a tropopause fold is occurring, while both trajectories enter the SPJ.

Supplemental movie S3 provides a more complete visual depiction for how low-ozone, boundary layer air is transported into juxtaposition with high-ozone air in the SPJ. Rowe and Hitchman (2015, 2016) and Hitchman and Rowe (2017) show examples of this process of fold formation during the Super Tuesday cyclone.

We hypothesize that the low ozone, low water, and weak or negative PV commonly found on the equatorward side of the jet is a result of the upstream injection of lower-tropospheric air by thunderstorms into the UTLS. Although we do not simulate convection upstream of the SPJ observed in RF04, satellite images show that there likely were convective injections of boundary layer air into the UTLS flow in the ridge, which were then advected eastward into proximity with the SPJ. RF01 provides a more direct example of this process, where convection occurred in closer proximity to the aircraft flight path.

Figure 13 shows an idealized diagram for how this can occur. Deep convection often occurs in the warm air mass to the south and east of an upper-level stratospheric PV intrusion or midlatitude cyclone, such as for RF01, and (one trough upstream) for RF04. The aggregation of poleward detrainment plumes of convective updraft air with low PV contribute to the creation and structure of an upper-level ridge (Shutts 1987; Fulton et al. 1995). Poleward plumes in the UTLS from tropical deep convection are crucial for determining the structure of the STJ (Nytes and Tripoli 2019). By similar reasoning, the time and space integral of air detrained from deep thunderstorms on the flank of the SPJ at all locations

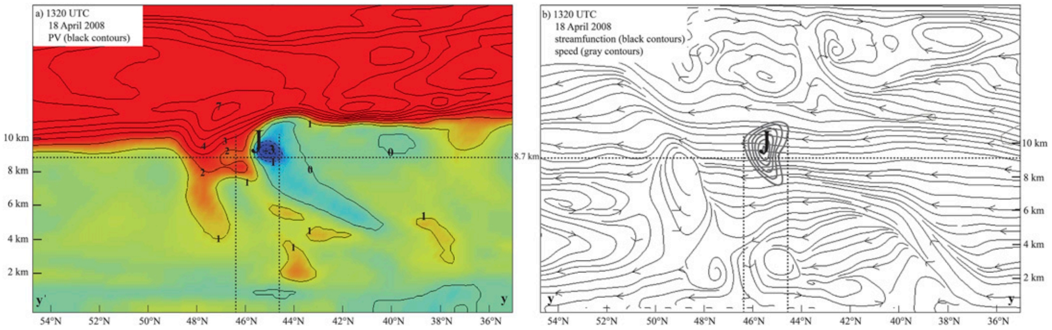

FIG. 11. Meridional sections along y–y′ in Fig. 10 during RF01 at 1320 UTC 18 Apr 2008 in the UWNMS. (a) PV (color fill, blue negative, with black contours every 1 PVU) and (b) streamfunction and wind speed (gray contours every 3 m s^{-1} from 40 m s^{-1}). The meridional extent of the 40 m s^{-1} isotach is highlighted with vertical dotted lines. The 8.7 km altitude level is shown with a horizontal dotted line.

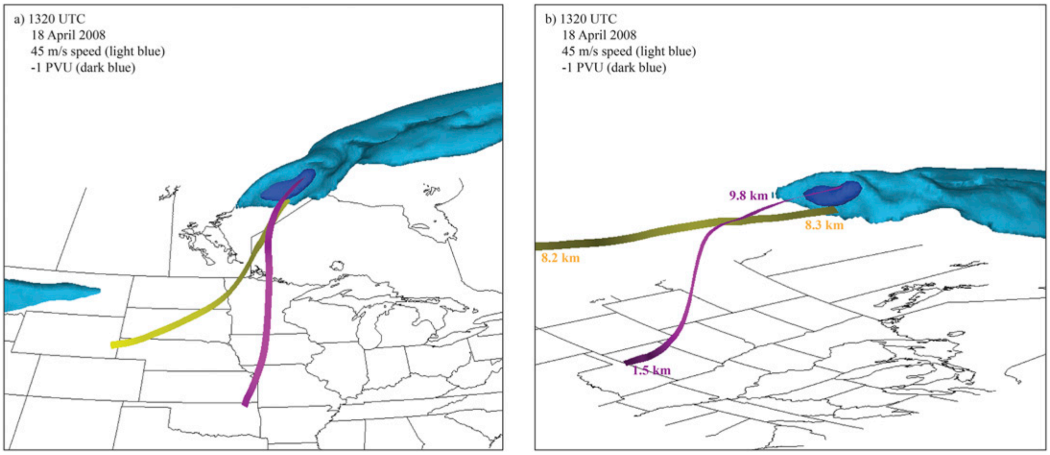

FIG. 12. Oblique views from the (a) south and (b) southeast of UWNMS 45 m s^{-1} wind speed isosurface (blue) and −1 PVU isosurface (dark blue) at 1320 UTC 18 Apr 2008. Two 26-h UWNMS trajectories are shown, with the purple one passing through the negative PV anomaly and the yellow one passing through the jet maximum in the UTLS over the upper Mississippi valley at 1320 UTC, illustrating rapid transport of lower-tropospheric air into the SPJ. The starting and ending altitudes are shown for the trajectories in (b). Supplemental movie S3 provides a more complete visualization of how upstream convection can enhance the constituent gradient near the SPJ.

upstream can help account for the sharpness of constituent gradients near the jet far downstream, such as where RF04 sampled the SPJ. The aggregate upper-level divergence resulting from the convection may be integral to the fundamental pattern of the fold itself, where upper-tropospheric air overrides stratospheric air at lower altitudes. Tropopause folds may be regarded ultimately as the combined effect of convective detrainment in the warm air mass and radiative cooling in the cold air mass.

7. Conclusions

The overall theme of this paper is to explore the role of differential advection in creating tropopause folds and constituent gradients in the UTLS associated with midlatitude jets and cyclones. Analysis of UWNMS simulations for RF04 shows that a tropopause fold (and jet superposition) can occur by quasi-isentropic differential advection in the vertical. Analysis of UWNMS simulations of RF01, RF04, and previously published cases show that differential advection associated with injection of boundary layer air by convection can explain the strong constituent gradient across the jet.

The mechanism of differential advection is distinct from the hypothesis that tropopause folds are due to a transverse circulation around the jet. An idealized sequence of events that can produce the classic cross section of a tropopause fold, purely by quasi-isentropic differential advection, is shown in Fig. 14. Just prior to RF04, a stratospheric PV anomaly was emplaced over the central United States, with no significant stratospheric folds, as shown in Figs. 14a and 14b. Then a jet streak in the upper troposphere propagated from the northwest along the upstream side of the trough, with flow near 10 km taking a more direct eastward course, overriding lower-stratospheric air in the 4–8 km layer (cf. Figs. 4a,c,e, and 14c). This created the classical signature in zonal section of a tropopause fold to the west of a trough (cf. Figs. 1a, 5b, and 14d).

One might imagine that, as a jet streak progressed cyclonically through the trough (Fig. 14e,f), a continuous "carving out" of the preexisting stratospheric PV anomaly would occur in the upper troposphere, creating a radially inward constriction

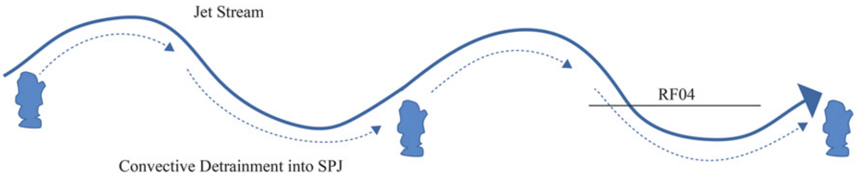

FIG. 13. Idealized plan view depicting injection of boundary layer air by thunderstorms into the SPJ at a range of locations upstream of an aircraft sampling location. The streamline indicates a sinusoidal westerly jet in the UTLS. Thunderstorm symbols indicate possible locations of injection of air into the SPJ. The bold horizontal line indicates a flight location, such as for RF04.

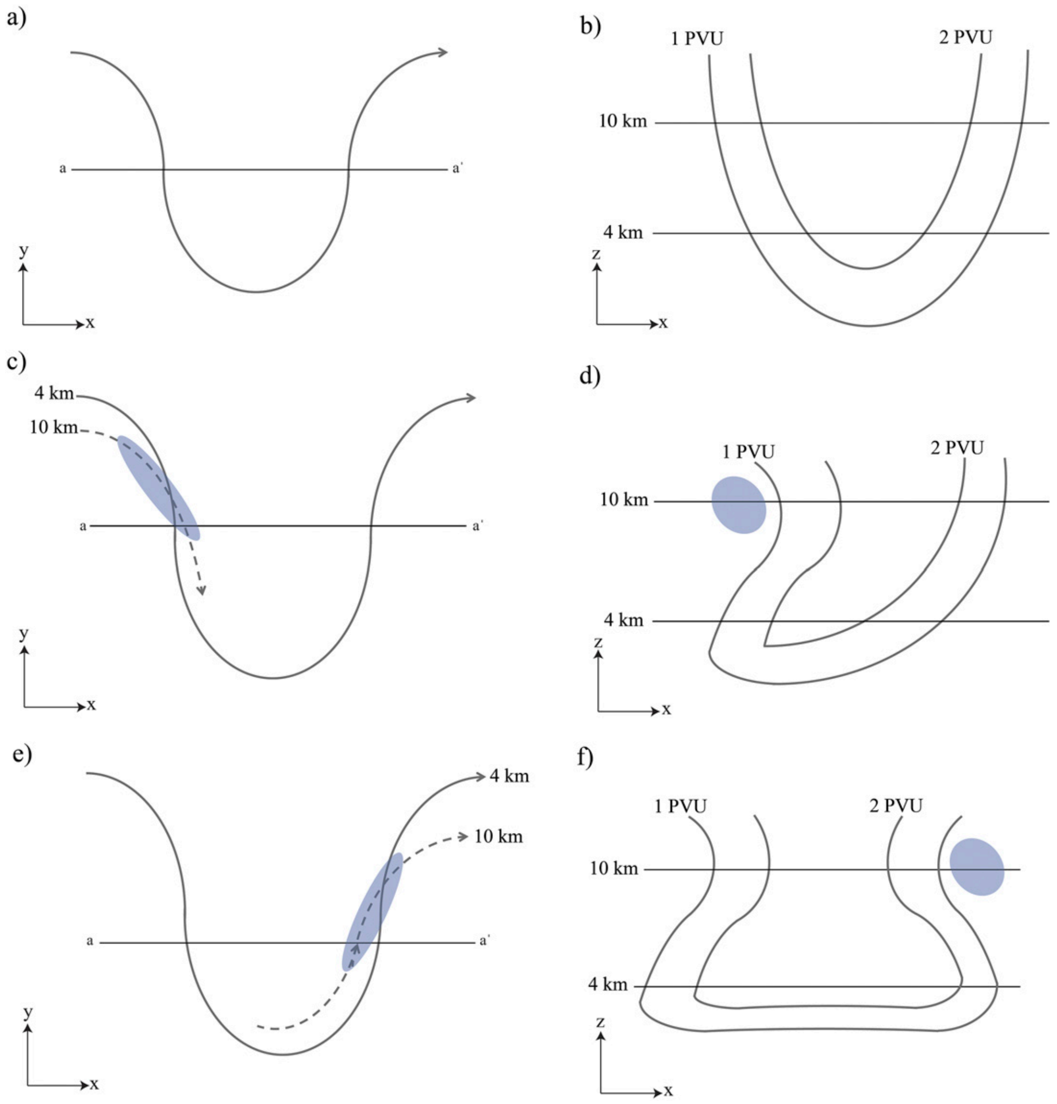

FIG. 14. Sequence of idealized (left) plan views and (right) zonal sections through a midlatitude cyclone showing how the classical signature of a tropopause fold may be produced by a jet streak of upper-tropospheric air in the SPJ. Consider a preexisting symmetric trough and stratospheric PV anomaly with (a) superimposed horizontal streamlines near 4 and 10 km and (b) two PV contours in a zonal section indicating the ULTS. (c) A momentum surge (oval speed maximum shown in blue) of upper-tropospheric air near 10 km can override lower-stratospheric air near 4 km on the upstream side of a trough, yielding (d) the signature of a tropopause fold to the west of the trough. (e) Continuation of a jet streak in the SPJ around the trough and poleward would produce (f) the symmetric pattern of tropopause fold common in cutoff lows (e.g., Fig. 1c).

of stratospheric PV near 10 km relative to 4–8 km. This situation is similar to that shown in Figs. 1c and 11a.

Although the dynamics underlying midlatitude jets, developing cyclones, and tropopause folds is complex, the fundamental concept of differential advection contributes toward understanding how tropopause folds are formed, how jets become superimposed, and how strong constituent gradients are produced near westerly jets. The jet streaks that override stratospheric air may have their origin in the aggregate divergent outflow from upstream convection.

Acknowledgments. We would like to acknowledge support from NSF Grants AGS-1256215 and AGS-1947658. We thank Elliot Shiben and Taylor Wilmot for helpful calculations and Michael Morgan for useful conversation. We would also like to thank the editor and reviewers for their helpful suggestions.

REFERENCES

Barth, M. C., J. Lee, A. Hodzic, G. Pfister, W. C. Skamarock, J. Worden, J. Wong, and D. Noone, 2012: Thunderstorms and upper troposphere chemistry during the early stages of the

2006 North American monsoon. *Atmos. Chem. Phys.*, **12**, 11 003–11 026, https://doi.org/10.5194/acp-12-11003-2012.

Bowman, K. P., L. L. Pan, T. Campos, and R. Gao, 2007: Observations of fine-scale transport structure in the upper troposphere from the High performance Instrumented Airborne Platform for Environmental Research. *J. Geophys. Res.*, **112**, D18111, https://doi.org/10.1029/2007JD008685.

Browell, E. V., E. F. Danielsen, S. Ismail, G. L. Gregory, and S. M. Beck, 1987: Tropopause fold structure determined from airborne lidar in situ measurements. *J. Geophys. Res.*, **92**, 2112–2120, https://doi.org/10.1029/JD092iD02p02112.

Bush, A. B. G., and W. R. Peltier, 1994: Tropopause folds and synoptic-scale baroclinic wave life cycles. *J. Atmos. Sci.*, **51**, 1581–1604, https://doi.org/10.1175/1520-0469(1994)051<1581:TFASSB>2.0.CO;2.

Christenson, C. E., J. E. Martin, and Z. J. Handlos, 2017: A synoptic climatology of Northern Hemisphere cold season polar and subtropical jet superposition events. *J. Climate*, **30**, 7231–7246, https://doi.org/10.1175/JCLI-D-16-0565.1.

Cooper, O., and Coauthors, 2004: On the life cycle of a stratospheric intrusion and its dispersion into polluted warm conveyor belts. *J. Geophys. Res.*, **109**, D23S09, https://doi.org/10.1029/2003JD004006.

Danielsen, E. F., 1968: Stratospheric–tropospheric exchange based on radioactivity, ozone and potential vorticity. *J. Atmos. Sci.*, **25**, 502–518, https://doi.org/10.1175/1520-0469(1968)025<0502:STEBOR>2.0.CO;2.

Eliassen, A., 1962: On the vertical circulation in frontal zones. *Geophys. Publ.*, **24**, 147–160.

——, and E. Kleinschmidt, 1957: Dynamic meteorology. *Geophysik II*, J. Bartels, Ed., Handbuch der Physik, Vol. 48, Springer-Verlag, 1–154.

Fulton, S. R., W. H. Schubert, and S. A. Hausman, 1995: Dynamical adjustment of mesoscale convective anvils. *Mon. Wea. Rev.*, **123**, 3215–3226, https://doi.org/10.1175/1520-0493(1995)123<3215:DAOMCA>2.0.CO;2.

Harvey, B., J. Methven, C. Sanchez, and A. Schaefler, 2020: Diabatic generation of negative potential vorticity and its impact on the North Atlantic jet stream. *Quart. J. Roy. Meteor. Soc.*, **146**, 1477–1497, https://doi.org/10.1002/qj.3747.

Hashino, T., and G. Tripoli, 2007: The Spectral Ice Habit Prediction System (SHIPS). Part I: Model description and simulation of vapor deposition process. *J. Atmos. Sci.*, **64**, 2210–2237, https://doi.org/10.1175/JAS3963.1.

Hegglin, M. I., and Coauthors, 2008: Validation of ACE-FTS satellite data in the upper troposphere/lower stratosphere (UTLS) using non-coincident measurements. *Atmos. Chem. Phys.*, **8**, 1483–1499, https://doi.org/10.5194/acp-8-1483-2008.

Hitchman, M. H., and A. S. Huesmann, 2007: A seasonal climatology of Rossby wave breaking in the 330–2000-K layer. *J. Atmos. Sci.*, **64**, 1922–1940, https://doi.org/10.1175/JAS3927.1.

——, and S. M. Rowe, 2017: On the similarity of lower-stratospheric potential vorticity dipoles above tropical and midlatitude deep convection. *J. Atmos. Sci.*, **74**, 2593–2613, https://doi.org/10.1175/JAS-D-16-0239.1.

——, and ——, 2019: On the structure and formation of UTLS PV dipole/jetlets in tropical cyclones by convective momentum surges. *Mon. Wea. Rev.*, **147**, 4107–4125, https://doi.org/10.1175/MWR-D-18-0232.1.

——, M. L. Büker, G. J. Tripoli, R. B. Pierce, J. A. Al-Saadi, E. V. Browell, and M. A. Avery, 2004: A modeling study of an East Asian convective complex during March 2001. *J. Geophys. Res.*, **109**, D15S14, https://doi.org/10.1029/2003JD004312.

Homeyer, C. R., K. P. Bowman, and L. L. Pan, 2010: Extratropical tropopause transition layer characteristics from high-resolution sounding data. *J. Geophys. Res.*, **115**, D13108, https://doi.org/10.1029/2009JD013664.

——, ——, ——, E. L. Atlas, R.-S. Gao, and T. L. Campos, 2011a: Dynamical and chemical characteristics of tropospheric intrusions observed during START08. *J. Geophys. Res.*, **116**, D06111, https://doi.org/10.1029/2010JD015098.

——, ——, ——, M. A. Zondlo, and J. F. Bresch, 2011b: Convective injection into stratospheric intrusions. *J. Geophys. Res.*, **116**, D23304, https://doi.org/10.1029/2011JD016724.

Hoor, P., H. Fischer, L. Lange, J. Lelieveld, and D. Brunner, 2002: Seasonal variations of a mixing layer in the lowermost stratosphere as identified by the CO-O_3 correlation from in situ measurements. *J. Geophys. Res.*, **107**, 4044, https://doi.org/10.1029/2000JD000289.

Hoskins, B. J., and F. P. Bretherton, 1972: Atmospheric frontogenesis models: Mathematical formulation and solution. *J. Atmos. Sci.*, **29**, 11–37, https://doi.org/10.1175/1520-0469(1972)029<0011:AFMMFA>2.0.CO;2.

——, and I. Draghici, 1977: The forcing of ageostrophic motion according to the semi-geostrophic equations and in an isentropic coordinate model. *J. Atmos. Sci.*, **34**, 1859–1867, https://doi.org/10.1175/1520-0469(1977)034<1859:TFOAMA>2.0.CO;2.

——, M. E. McIntyre, and A. W. Robertson, 1985: On the use and significance of isentropic potential vorticity maps. *Quart. J. Roy. Meteor. Soc.*, **111**, 877–946, https://doi.org/10.1002/qj.49711147002.

Huntrieser, H. M., and Coauthors, 2016a: Injection of lightning-produced NOx, water vapor, wildfire emissions, and stratospheric air to the UT/LS as observed from DC3 measurements. *J. Geophys. Res.*, **121**, 6638–6668, https://doi.org/10.1002/2015JD024273.

——, and Coauthors, 2016b: On the origin of pronounced O_3 gradients in the thunderstorm outflow region during DC3. *J. Geophys. Res.*, **121**, 6600–6637, https://doi.org/10.1002/2015JD024279.

Jourdain, L., S. S. Kulawik, H. M. Worden, K. E. Pickering, J. Worden, and A. M. Thompson, 2010: Lightning NOx emissions over the USA constrained by TES ozone observations and the GEOS-Chem model. *Atmos. Chem. Phys.*, **10**, 107–119, https://doi.org/10.5194/acp-10-107-2010.

Knox, J. A., and V. L. Harvey, 2005: Global climatology of inertial instability and Rossby wave breaking in the stratosphere. *J. Geophys. Res.*, **110**, D06108, https://doi.org/10.1029/2004JD005068.

Madonna, E., H. Wernli, H. Joos, and O. Martius, 2014: Warm conveyor belts in the ERA-Interim data set (1979–2010). Part I: Climatology and potential vorticity evolution. *J. Climate*, **27**, 3–26, https://doi.org/10.1175/JCLI-D-12-00720.1.

Martínez-Alvarado, O., H. Joos, J. Chagnon, M. Boettcher, S. L. Gray, R. S. Plant, J. Methven, and H. Wernli, 2014: The dichotomous structure of the warm conveyor belt. *Quart. J. Roy. Meteor. Soc.*, **140**, 1809–1824, https://doi.org/10.1002/qj.2276.

Martius, O., C. Schwartz, and H. C. Davies, 2007: Breaking waves at the tropopause in the wintertime Northern Hemisphere: Climatological analysis of the orientation and the theoretical

LC1/2 classification. *J. Atmos. Sci.*, **64**, 2576–2592, https://doi.org/10.1175/JAS3977.1.

McIntyre, M. E., and T. N. Palmer, 1983: Breaking planetary waves in the stratosphere. *Nature*, **305**, 593–600, https://doi.org/10.1038/305593a0.

Nytes, L. E., and G. J. Tripoli, 2019: Seasonal and subseasonal variability of potential energy injected into the tropical UTLS by convective and tropical cyclone outflow. *J. Climate*, **32**, 8003–8017, https://doi.org/10.1175/JCLI-D-18-0303.1.

O'Sullivan, D. J., and T. J. Dunkerton, 1995: Generation of inertia–gravity waves in a simulated life cycle of baroclinic instability. *J. Atmos. Sci.*, **52**, 3695–3716, https://doi.org/10.1175/1520-0469(1995)052<3695:GOIWIA>2.0.CO;2.

Pan, L. L., and Coauthors, 2007: Chemical behavior of the tropopause observed during the Stratosphere-Troposphere Analyses of Regional Transport experiment. *J. Geophys. Res.*, **112**, D18110, https://doi.org/10.1029/2007JD008645.

——, and Coauthors, 2010: The Stratosphere–Troposphere Analyses of Regional Transport 2008 experiment. *Bull. Amer. Meteor. Soc.*, **91**, 327–342, https://doi.org/10.1175/2009BAMS2865.1.

——, and Coauthors, 2014: Thunderstorms enhance tropospheric ozone by wrapping and shedding stratospheric air. *Geophys. Res. Lett.*, **41**, 7785–7790, https://doi.org/10.1002/2014GL061921.

Phoenix, D. B., C. R. Homeyer, M. C. Barth, and S. B. Trier, 2020: Mechanisms responsible for stratosphere-to-troposphere transport around a mesoscale convective system anvil. *J. Geophys. Res. Atmos.*, **125**, e2019JD032016, https://doi.org/10.1029/2019JD032016.

Pittman, J. V., and Coauthors, 2009: Evaluation of AIRS, IASI, and OMI ozone profile retrievals in the extratropical tropopause region using in situ aircraft measurements. *J. Geophys. Res.*, **114**, D24109, https://doi.org/10.1029/2009JD012493.

Randel, W. J., and E. J. Jensen, 2013: Physical processes in the tropical tropopause layer and their roles in changing climate. *Nat. Geosci.*, **6**, 169–176, https://doi.org/10.1038/ngeo1733.

——, D. J. Seidel, and L. L. Pan, 2007: Observational characteristics of double tropopauses. *J. Geophys. Res.*, **112**, D07309, https://doi.org/10.1029/2006JD007904.

Rayleigh, L., 1916: On the dynamics of revolving fluids. *Proc. Roy. Soc. London*, **92A**, 148–154, https://doi.org/10.1098/rspa.1917.0010.

Reed, R. J., 1955: A study of a characteristic type of upper level frontogenesis. *J. Meteor.*, **12**, 226–237, https://doi.org/10.1175/1520-0469(1955)012<0226:ASOACT>2.0.CO;2.

Rotunno, R., W. C. Skamarock, and C. Snyder, 1994: An analysis of frontogenesis in numerical simulations of baroclinic waves. *J. Atmos. Sci.*, **51**, 3373–3398, https://doi.org/10.1175/1520-0469(1994)051<3373:AAOFIN>2.0.CO;2.

Rowe, S. M., and M. H. Hitchman, 2015: On the role of inertial instability in stratosphere–troposphere exchange in midlatitude cyclones. *J. Atmos. Sci.*, **72**, 2131–2151, https://doi.org/10.1175/JAS-D-14-0210.1.

——, and ——, 2016: On the relationship between inertial instability, poleward momentum surges and jet intensifications near midlatitude cyclones. *J. Atmos. Sci.*, **73**, 2299–2315, https://doi.org/10.1175/JAS-D-15-0183.1.

——, and ——, 2020: The destruction of a stratospheric potential vorticity intrusion due to inertial instability in the UTLS as it relates to the 20 August 2018 southern Wisconsin extreme flooding event. *Mon. Wea. Rev.*, **148**, 4397–4414, https://doi.org/10.1175/MWR-D-19-0213.1.

Sato, K., and T. J. Dunkerton, 2002: Layered structure associated with low potential vorticity near the tropopause seen in high-resolution radiosondes over Japan. *J. Atmos. Sci.*, **59**, 2782–2800, https://doi.org/10.1175/1520-0469(2002)059<2782:LSAWLP>2.0.CO;2.

Sawyer, J. S., 1956: The vertical circulation at meteorological fronts and its relation to frontogenesis. *Proc. Roy. Soc. London*, **234A**, 346–362, https://doi.org/10.1098/rspa.1956.0039.

Schoeberl, M. R., and A. E. Dessler, 2011: Dehydration of the stratosphere. *Atmos. Chem. Phys.*, **11**, 8433–8446, https://doi.org/10.5194/acp-11-8433-2011.

——, E. J. Jensen, L. Pfister, R. Ueyama, M. Avery, and A. E. Dessler, 2018: Convective hydration of the upper troposphere and lower stratosphere. *J. Geophys. Res.*, **123**, 4583–4593, https://doi.org/10.1029/2018JD028286.

Schroeder, J. R., and Coauthors, 2014: Evidence of mixing between polluted convective outflow and stratospheric air in the upper troposphere during DC3. *J. Geophys. Res. Atmos.*, **119**, 11 477–11 491, https://doi.org/10.1002/2014JD022109.

Shapiro, M. A., 1978: Further evidence of the mesoscale and turbulent structure of upper level jet stream–frontal zone systems. *Mon. Wea. Rev.*, **106**, 1100–1111, https://doi.org/10.1175/1520-0493(1978)106<1100:FEOTMA>2.0.CO;2.

——, 1980: Turbulent mixing within tropopause folds as a mechanism for the exchange of chemical constituents between the stratosphere and troposphere. *J. Atmos. Sci.*, **37**, 994–1004, https://doi.org/10.1175/1520-0469(1980)037<0994:TMWTFA>2.0.CO;2.

Shutts, D. J., 1987: Balanced flow states resulting from penetrative, slantwise convection. *J. Atmos. Sci.*, **44**, 3363–3376, https://doi.org/10.1175/1520-0469(1987)044<3363:BFSRFP>2.0.CO;2.

Sprenger, M., and H. Wernli, 2003: A Northern Hemispheric climatology of cross-tropopause exchange for the ERA15 time period (1979–1993). *J. Geophys. Res.*, **108**, 8521, https://doi.org/10.1029/2002JD002636.

——, ——, and M. Bourqui, 2007: Stratosphere–troposphere exchange and its relation to potential vorticity streamers and cutoffs near the extratropical tropopause. *J. Atmos. Sci.*, **64**, 1587–1602, https://doi.org/10.1175/JAS3911.1.

Stohl, A., and Coauthors, 2003: Stratosphere-troposphere exchange: A review, and what we have learned from STACCATO. *J. Geophys. Res.*, **108**, 8516, https://doi.org/10.1029/2002JD002490.

Taylor, G. I., 1923: Stability of a viscous liquid contained between two rotating cylinders. *Phil. Trans. Roy. Soc. London*, **223A**, 289–343, https://doi.org/10.1098/rsta.1923.0008.

Thompson, C. F., D. M. Schultz, and G. Vaughan, 2018: A global climatology of tropospheric inertial instability. *J. Atmos. Sci.*, **75**, 805–825, https://doi.org/10.1175/JAS-D-17-0062.1.

Thorncroft, C. D., B. J. Hoskins, and M. E. McIntyre, 1993: Two paradigms of baroclinic wave life cycle behavior. *Quart. J. Roy. Meteor. Soc.*, **119**, 17–55, https://doi.org/10.1002/qj.49711950903.

Tripoli, G. J., 1992: A nonhydrostatic numerical model designed to simulate scale interaction. *Mon. Wea. Rev.*, **120**, 1342–1359, https://doi.org/10.1175/1520-0493(1992)120<1342:ANMMDT>2.0.CO;2.

Wandishin, M. S., J. W. Nielsen-Gammon, and D. Keyser, 2000: A potential vorticity diagnostic approach to upper-level frontogenesis within a developing baroclinic wave. *J. Atmos. Sci.*, **57**, 3918–3938, https://doi.org/10.1175/1520-0469(2001)058<3918:APVDAT>2.0.CO;2.

Winters, A. C., and J. E. Martin, 2016: Synoptic and mesoscale processes supporting vertical superposition of the polar and subtropical jets in two contrasting cases. *Quart. J. Roy. Meteor. Soc.*, **142**, 1133–1149, https://doi.org/10.1002/qj.2718.

——, and ——, 2017: Diagnosis of a North American polar–subtropical jet superposition employing piecewise potential vorticity inversion. *Mon. Wea. Rev.*, **145**, 1853–1873, https://doi.org/10.1175/MWR-D-16-0262.1.

Zahn, A., and Coauthors, 2000: Identification of extratropical two-way troposphere-stratosphere mixing based on CARIBIC measurements of O_3, CO, and ultrafine particles. *J. Geophys. Res.*, **105**, 1527–1535, https://doi.org/10.1029/1999JD900759.